Enhancing anti-tumor immunity through liposomal oxaliplatin and localized immunotherapy via STING activation

Gu, Z.L.; Hao, Y.; Schomann, T.; Ossendorp, F.; Dijke, P. ten; Cruz, L.J.

Journal of Controlled Release 357 (2023) 531–544

Contents lists available at ScienceDirect

Journal of Controlled Release

journal homepage: www.elsevier.com/locate/jconrel

Enhancing anti-tumor immunity through liposomal oxaliplatin and localized immunotherapy *via* STING activation

Zili Gu [a], Yang Hao [a,b,c], Timo Schomann [a,d], Ferry Ossendorp [e], Peter ten Dijke [c,*], Luis J. Cruz [a,*]

[a] Department of Radiology, Leiden University Medical Center, the Netherlands
[b] Department of Laboratory Animals, College of Animal Sciences, Jilin University, Changchun, China
[c] Oncode Institute, Department of Cell and Chemical Biology, Leiden University Medical Center, the Netherlands
[d] Department of Vascular Surgery, Leiden University Medical Center, the Netherlands
[e] Department of Immunology, Leiden University Medical Center, the Netherlands

ARTICLE INFO

Keywords:
Liposomes
Nanomedicine
Immunochemotherapy
STING
Oxaliplatin
Cancer

ABSTRACT

The cyclic GMP-AMP synthase-stimulator of interferon genes (cGAS-STING) pathway is a promising approach for anti-cancer immunotherapy by bridging innate and adaptive immunity. Recent evidence suggests that chemotherapy-induced DNA damage can directly induce dendritic cell (DC) maturation and recruitment, which synergizes with STING activation to enhance anti-tumor effects. As an immunogenic cell death (ICD) inducer, oxaliplatin generates massive double-stranded DNA (dsDNA) crosslinks, release of tumor-associated antigens and promoting the "eat me" signal. STING activation improves antigen immunogenicity, which can promote T cell activation and infiltration. In this study, we developed liposomes encapsulating oxaliplatin and combine this formulation with a STING agonist (ADU-S100) for treating colorectal cancer. The liposomes efficiently inhibited the proliferation of tumor cells while induced ICD in CT26 colorectal cancer cells, which enhanced dendritic cell maturation and phagocytosis *in vitro*. The liposome-based immunochemotherapy exhibited the strongest efficacy, resulting in complete remission upon tumor inoculation. Mechanistic studies showed this potent anti-cancer effect was related to the significant recruitment of infiltrating CD8 and CD4 T cells, reduction of suppressive Treg cells, and a shift in the phenotype of tumor-associated suppressive macrophages that promote cancer to immune stimulating macrophages. Thus, our study demonstrated the potential of combining oxaliplatin-loaded liposomes with a STING agonist to reduce tumor growth by regulating the immunosuppressive state in the tumor.

1. Introduction

Cancer immunotherapy has revolutionized the field of oncology by eradicating malignant cells or modifying the phenotype and functions of immune cells [1–3]. Various types of cancer, such as non-small cell lung cancer, colorectal cancer, melanoma, and others. [4–6], have shown effective clinical responses to immunotherapy. In cancer immunotherapy, several strategies are employed to enhance immune activation or normalize tumor-induced deficiency, thereby eliciting a potent immune response. Notably, the majority of these strategies aim on boosting the adaptive branch of the immune system. Recently, research community has reached a consensus that bridging the gap between treatment targeted at adaptive immunity and innate immunity may efficiently improve anti-tumor effects [7]. Specifically, both the innate and adaptive branches of immune system should be engaged to achieve sufficient immune response [8], therefore, more and more attention

Abbreviations: ATP, adenosine triphosphate; BSA, bovine serum albumin; cGAS, cyclic GMP-AMP synthase; CFMDA, 1, 5-chloromethylfluorescein diacetate; CRT, calreticulin; CTL, cytotoxic T lymphocytes; DAMPs, damage-associated molecular patterns; DAPI, 4′,6-diamidino-2-phenylindole; DC, dendritic cell; DL, drug loading; dsDNA, double-stranded DNA; DSPC, 1,2-distearoyl-sn-glycero-3-phosphocholine; EE, encapsulation efficiency; eLP, empty liposomes; H&E, hematoxylin and eosin; HMGB1, high mobility group box 1; ICD, immunogenic cell death; IC_{50}, half maximal inhibitory concentration; IL, interleukin; IR780-LP, IR780-loaded liposomes; mPEG2000-DSPE, methoxy-polyethylene glycol (MW 2000)-distearoylphosphatidyl-ethanoloamine; MHC, major histocompatibility complex; OLP, oxaliplatin-loaded liposomes; OXA, oxaliplatin solution; STING, stimulator of interferon genes; TAA, tumor-associated antigens; TAMs, tumor-associated macrophages; TME, tumor microenvironment; Tregs, regulatory T lymphocytes; UPLC, high-performance liquid chromatography..

* Corresponding author.
E-mail addresses: P.ten_Dijke@lumc.nl (P. ten Dijke), l.j.cruz_ricondo@lumc.nl (L.J. Cruz).

https://doi.org/10.1016/j.jconrel.2023.04.011
Received 9 March 2023; Received in revised form 29 March 2023; Accepted 5 April 2023
Available online 21 April 2023

have been paid to this field.

Serveral studies have described the underlying mechanisms of how the cyclic GMP-AMP synthase-stimulator of interferon genes (cGAS-STING) pathway regulates tumor progression. It has been reported that STING pathway responds to damage-associated molecular patterns (DAMPs) or pathogen-associated molecular patterns and serves as a bridge role between innate and adaptive immunity. Upon STING activation, tumor microenvironment (TME) tends to be regulated and restored to an actively 'hot' tumor, which is beneficial for overcoming immune escape developed by tumors [9–11]. Specifically, the activation of STING in tumor cells directly induces death modality (apoptosis, necroptosis, *etc.*) [12], while also increases the sensitivity of tumor cells to cytotoxic T lymphocytes (CTL) and eliminates the suppressive immune cells within the TME [13]. Furthermore, STING activation also improves antigen immunogenicity by stimulating immunogenic cell death (ICD), promotes dendritic cell (DC) maturation and presentation, primes and recruits T cells, and thereby enhances CTL killing ability [14–16]. This knowledge revealed a possibility to combine immunochemotherapy with chemotherapy since chemotherapy was reported to offer sufficient tumor-specific antigens or tumor-associated antigens (TAA) for STING agonists-induced anti-tumor immunity, which allows the whole tumor to be transformed into a vaccine [17].

Recent evidence suggests that addition to tumor cell-produced ssDNA or dsDNA (*e.g.*, genomic instability), chemotherapy-induced DNA damage could directly induce DCs maturation and recruitment, potentially synergizing with STING activation [18–20]. Oxaliplatin, a third-generation platinum-based cytotoxic drug commonly used in multiple cancers including colorectal cancer, acts by damaging the structure of DNA. It has been shown that oxaliplatin can promote the release of 1) TAAs as a typical ICD inducer, including calreticulin (CRT), adenosine triphosphate (ATP) and high mobility group box 1 (HMGB1) protein [21,22], and 2) double stranded DNA (dsDNA) fragments due to the induction of intracellular crosslinks [23,24]. Subsequently, these signals initiate the anti-tumor immunity. In addition, oxaliplatin treatment of tumor-bearing mice resulted in a remarkable decrease of M1-type tumor-associated macrophages (TAMs) in the tumor site [25], while STING agonist was reported to repolarize TAMs from the M2 type towards M1 type through type I interferon (IFN) upregulation [26,27]. With the normalization of tumor microenvironment (TME), STING agonist tends to strengthen the anti-tumor effect of oxaliplatin.

Although oxaliplatin has such potential for cancer treatment, its efficacy is limited mainly by severe side effects such as neuropathy and fast clearance from the blood circulation. Therefore, there is an urgent need to deliver anti-cancer agents precisely into the tumor tissue and minimize the side effects. As the firstly applied nanotherapeutics applied in the clinic, liposomes have shown potential for delivering a variety of anti-cancer agents, including small molecules, oligonucleotides, peptides, and proteins, *etc.* [28,29]. Many studies have demonstrated that liposome is an ideal nanocarrier platform due to its unique properties, such as high biocompatibility, low immunogenicity, high delivery

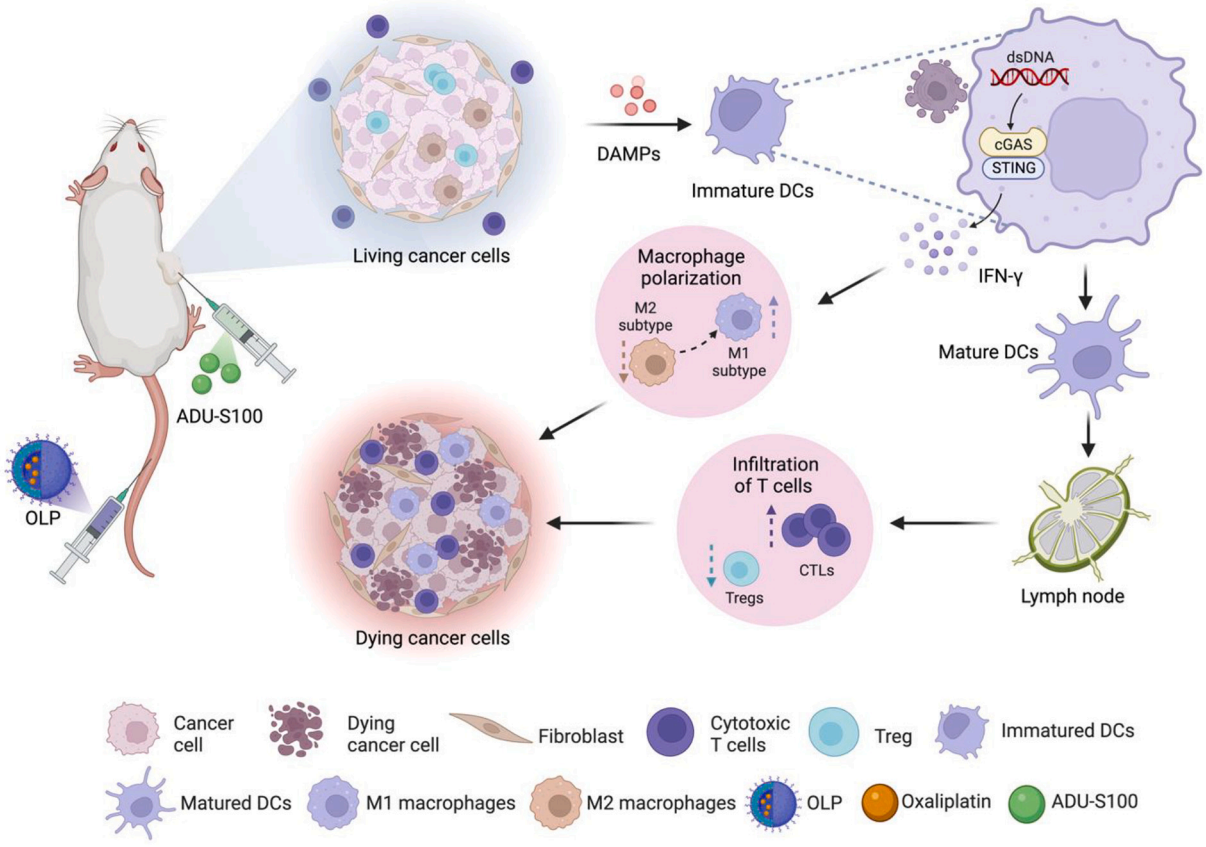

Fig. 1. The schematic illustration of liposome-mediated immunochemotherapy. This figure depicts a schematic representation of liposome-mediated immunochemotherapy. The liposomes (OLP) are shown as spherical structures enclosing therapeutic agents such as the chemotherapeutic drug oxaliplatin (OXA) and the STING agonist ADU-S100. The liposomes are designed to target the tumor cells specifically and facilitate the delivery of the therapeutic agents to the TME. Upon reaching the TME, the liposomes are taken up by the tumor cells and the therapeutic agents are released into the surrounding area. The release of OXA triggers the immunogenic cell death of the tumor cells, which further activates the immune system. Meanwhile, the released ADU-S100 activates the STING pathway, promoting the production of type I interferons and cytokines. This results in the recruitment of immune cells such as DCs, which prime T cells for a specific anti-tumor response. The liposome-mediated immunochemotherapy not only enhances the anti-tumor immune response, but also reduces the recruitment of M2 macrophages and regulatory T lymphocytes (Tregs) in the TME. These combined effects of liposome-mediated immunochemotherapy result in a more effective and targeted approach for cancer treatment.

efficiency, long circulation ability, *etc.* In addition, liposomes have an aqueous core that can encapsulate hydrophilic drugs, which makes them suitable carriers for the delivery of oxaliplatin.

We present a novel approach to cancer treatment using liposome-mediated immunochemotherapy. Liposomes serve as a nanocarrier to deliver oxaliplatin to the tumor site, followed by subsequent STING activation to achieve a potent anti-tumor effect (Fig. 1). We chose CT26 colorectal cancer for this study because oxaliplatin exposure could release tumor-associated antigens (TAAs) and double-stranded DNA, which favor dendritic cell activation and T cell-mediated killing [30,31]. Mechanistically, these signals synergize with ADU-S100 (STING agonist) and boost the immune response. To the best of our knowledge, this is the first study combining oxaliplatin and ADU-S100 for cancer therapy, and the use of liposomes further amplifies their anti-cancer effects. Our strategy demonstrates efficient delivery of oxaliplatin with STING activation, which could greatly facilitate its clinical translation for cancer treatment.

2. Materials and methods

2.1. Materials

Methoxy-polyethylene glycol (MW 2000)-distearoylphosphatidyl-ethanoloamine (mPEG2000-DSPE), 1,2-distearoyl-sn-glycero-3-phosphocholine (DSPC), and cholesterol were purchased from Avanti® Polar Lipids (Alabaster, USA). Oxaliplatin was obtained from EDQM (Strasbourg, France). ADU-S100 was acquired from MedChemExpress (NJ, USA).

2.2. Cell lines

The CT26 cell line (mouse colorectal cells) was donated by Dr. Candido Silva and maintained in IMDM medium supplemented with 10% fetal bovine serum, 100 U/mL penicillin, and 100 μg/mL streptomycin. The cells were cultured under the controlled condition of 37 °C and 5% CO_2.

2.3. Animals

Female BALB/c mice were purchased from ENVIGO (Limburg, the Netherlands), and housed in pathogen-free animal facilities at Leiden University Medical Center (LUMC). All experimental animals were 6–8 weeks old unless otherwise stated. All animal experiments were performed under Dutch Animal Ethics Committee's Code of Conduct and Dutch animal welfare laws. The local animal welfare body of the LUMC reviewed and approved all animal studies (project number: AVD116008045).

2.4. Preparation of liposomes

The preparation of liposomes involved dissolving DSPC:cholesterol: DSPE-PEG2000 in a molar ratio of 55:30:4 in chloroform, followed by evaporating the solvent to obtain a lipid film. The film was then dried overnight in a vacuum desiccator to remove residual chloroform and then hydrated with 1.5 mg/mL oxaliplatin-contained 5% glucose at 65 °C for 1 h to form the final lipid suspension. Subsequently, the suspension was subsequently extruded through two stacked polycarbonate membranes (Whatman®, NucleporeTM, GE Healthcare, Little Chalfont, UK) of 400 nm and 200 nm using a LIPEX Extruder. (LIPEX Extruder, Northern Lipids Inc., Burnaby, Canada). To remove the unloading oxaliplatin, Amicon Ultra 15 (300,000 Da, Milipore, Darmstadt, Germany) was centrifuged at 4000*g* for 1 h. The resulting liposomes were stored at 4 °C until use. IR780-loaded liposomes (IR780-LP) were prepared using IR780 as a fluorescence marker under the same conditions but in darkness.

2.5. Characterization of the liposomes

Particle size and distribution and ζ-potential was measured by using dynamic light scattering on a Zetasizer Nano ZS90 instrument (Malvern Instruments, Malvern, London, UK). The morphological properties of the liposomes were evaluated by transmission electron microscopy (TEM, Tecnai 12 Twin, FEI Company; Hillsboro, Oregon, USA) with an accelerating voltage of 120 kV, which was stained with 2% uranyl acetate in distilled water. The encapsulation efficiency (EE%) and drug loading (DL%) of oxaliplatin were determined by ultra-high-performance liquid chromatography (UPLC, Waters, Milford, MA, USA). To determine the encapsulated oxaliplatin in liposomes, we added methanal, ultrasonicated the mixture for 15 min, filtered the mixture through a 0.22-μm organic filter, finally, analyzed them by UPLC with a C18 column (ACQUITY, C18, 100 mm × 2.1 mm, 1.7 μm) at room temperature with a UV absorption wavelength of 250 nm.

The dynamic dialysis method was employed to evaluate the oxaliplatin release profile under physiological pH conditions *in vitro*. Samples were placed into dialysis bags with a molecular weight cutoff of 3.5 kDa (Thermo Fisher, MA, USA) and dialyzed against PBS (pH 7.4). The dialysis bag was then stirred at 100 rpm at 37 °C, and 500 μL of dialysate was removed from the sample at pre-determined time points. An equivalent volume of fresh medium was replenished to maintain a constant volume. The released oxaliplatin concentration was quantified using UPLC with a Waters ACQUITY system.

2.6. Cellular internalization

The fluorescence probe IR780 was used to investigate cellular drug uptake. We seeded CT26 cells in 24-well plates with a density of 30,000 cells per well in a complete medium with 10% fetal bovine serum and incubated overnight. After washing twice with PBS, cells were treated with IR780 and IR780-LP at 37 °C for 4 h with a final IR780 concentration of 1.25, 5, or 20 μg/mL. To determine the uptake efficiency, the cells were detached with 200 μL of trypsin-EDTA solution, centrifuged at 1000 rpm for 5 min, transferred to flow tubes (Falcon, Corning, New York, USA), resuspended in FACS buffer, and analyzed by flow cytometry (LSR-II, BD Biosciences, NJ, USA). Each experiment was repeated three times independently, and the data were analyzed with FlowJo 10.0 software.

To observe the cellular localization, we cultured cells with rhodamine-labeled liposomes (1% molar ratio) and captured them by means of confocal laser scanning microscopy (Leica SP5, Germany). Briefly, after two pre-cold PBS washes, the cells were then stained with different dyes for visualization. We investigated the distribution of liposomes within the lysosome, mitochondrion, endoplasmic reticulum (ER), and Golgi apparatus by using LysoTrack™ Green DND-26 (Invitrogen, Waltham, MA, USA), MitoTracker™ DeepRed (Invitrogen), ER-Tracker™ Green (Invitrogen), and BODIPY™ FL C5-Ceramide (Invitrogen). The incubation dose and time were as following: LysoTrack™ Green DND-26 (50 nM, 37 °C, 30 min), MitoTracker™ DeepRed (50 nM,37 °C, 30 min), ER-Tracker™ Green (1:1000, 37 °C, 30 min), and BODIPY™ FL C5-Ceramide (1:100, 4 °C,30 min). In addition, Hoechst 33342 (Thermo Fisher) was used for staining of nuclei with a dilution of 1:1000 for 5 min. All the staining was performed according to the manufacturer's protocols.

2.7. Cytotoxicity assay in vitro

The *in vitro* cytotoxicity of free drug and liposomal formulations was evaluated using the MTS colorimetric assay, following the manufacturer's protocol (Promega, the Netherlands). CT26 cells were cultured in 96-well plates with a density of 5000 cells per well in 100 μL of complete medium and incubated overnight at 37 °C. We measured the cytotoxicity of empty liposomes (eLP), oxaliplatin solution (OXA), oxaliplatin-loaded liposomes (OLP), as well as a control group (an equivalent volume of

blank complete medium). These groups were added to the wells in designated concentrations of oxaliplatin (0.0005, 0.0025, 0.0128, 0.064, 0.32, 1.6, 8, 40 μg/mL) and eLP (lipid concentration: 0.16, 0.8, 4, 20, 100, 500 μg/mL). Next, the cells were incubated at 37 °C and 5% CO_2 for 24 h and 48 h. Subsequently, 20 μL of MTS was added to each well, followed by a 1.5 h incubation period, and the optical density (OD) was recorded at 490 nm using SpectraMax ABS Plus (Molecular Devices, San Jose, CA, USA). This experiment was repeated three times independently, and the half maximal inhibitory concentration (IC_{50}) was determined using GraphPad Prism 9.0 software.

To assess the apoptosis induced by different treatments, CT26 cells were cultured in 24-well plates at a density of 20,000 cells per well. After co-culture with the free oxaliplatin or liposomal formulations, the cells were harvested using EDTA-free trypsin, washed with precooled PBS, and resuspended in the binding buffer. Next, Annexin V-PE (5 μL, Biolegend, San Diego, USA) was added to the cells and incubated in the dark for 15 min, followed by 4′,6-diamidino-2-phenylindole (DAPI, Thermo Fisher) (10 μL) for 5 min. The treated cells were then transferred to a flow cytometry tube and analyzed within 30 min using a LSR II flow cytometer (BD Biosciences, USA).

2.8. DC activation study

DC activation was performed to verify the activity of ADU-S100 and optimize the ideal dose for further assay. We treated D1 DCs in designated concentrations of ADU-S100 (3.125, 6.25, 12.5, 25, 50, 100, 200 ng/mL) for 24 h. After incubation, PBS/EDTA (Sigma-Aldrich, St. Louis, USA) was used to detach D1 DCs, which were then washed in FACS buffer and labeled with the following antibodies on the ice: anti-CD11c-APC-eF780 (clone N418, Thermo Fisher Scientific), anti-CD40-APC (clone 3/23, Biolegend), anti-CD86-PE-cy7 (clone GL1, BD Biosciences), and anti-I-Ab (major histocompatibility complex, MHC class II; Clone M5/114.15.2, Thermo Fisher Scientific). Following a 30-min staining, cells were washed in FACS buffer to remove unattached antibodies before being resuspended in 100 μL of the FACS buffer. Flow cytometry (LSR-II, BD Biosciences, USA) was used to measure DC maturation, and FlowJo 10.0 software was used to analyze the results.

2.9. Investigation of immunogenic cell death

To evaluate the immunogenic cell death, we assessed the expression of CRT on the cell surface, the release of ATP and HMGB1 protein. Briefly, 5000 CT26 cells were treated with different concentrations of OXA or OLP for 24 h. Afterward, we added RealTime-Glo™ Extracellular ATP Assay Reagent (Promega) to all the wells and gently mixed the plate. The luminescence intensity of extracellular ATP was measured using a SpectraMax iD3 (Molecular Devices, San Jose, CA, USA). The quantification of CRT was performed under the same treatment but measured by flow cytometry (LSR II, BD Bioscience) after cells were washed three times and stained with Alex Fluo647-labeled CRT (Clone 1G6A7, Novus Biologicals, Englewood, USA). To detect the release of the HMGB1, cells were fixed with 4% paraformaldehyde, permeabilized with 0.5% Triton-X100 (Sigma-Aldrich) in PBS for 5 min, and then treated with 5 μg/mL anti-HMGB1 (Novus Biologicals) at 4 °C overnight. The presence of the antibody was identified by staining with the secondary anti-rabbit Alex Fluo488 (Invitrogen) at a 1:500 dilution, and the level of HMGB1 were visualized using a DMB6 (Leica, Germany).

2.10. Co-culture study on DC maturation and phagocytosis

To assess the immunological effects of liposomes on immune cells, we labeled the CT26 cancer cells with 1, 5-chloromethylfluorescein diacetate (CFMDA) (Invitrogen) according to the manufacturer's instructions. D1DCs and pre-treated cancer cells were co-cultured with a ratio of 1:5 in 24-well plates for 24 h. Thereafter, we collected supernatants to measure interleukin (IL)-12 by IL-12p40 sandwich ELISA kit (Biolegend). The remaining D1DCs were harvested for FACS analysis. Cells were detached, washed, and stained with the following antibodies: anti-CD11c-APC-eF780 (clone N418, Thermo Fisher Scientific), anti-CD40-APC (clone 3/23, Biolegend), anti-CD86-PE-cy7 (clone GL1, BD Biosciences), and anti-I-Ab (MHC class II; clone M5/114.15.2, Thermo Fisher Scientific). DAPI was used to distinguish between live and dead cells. Cells were washed and resuspended with FACS buffer before being analyzed by flow cytometry (LSR-II, BD Biosciences, USA). Data were analyzed using FlowJo 10.0 software. All the experiments were independently repeated three times.

2.11. Xenograft tumor mouse model of colorectal cancer and biodistribution analysis

To establish an *in vivo* colorectal cancer model, 1×10^5 CT26 cells were injected subcutaneously into the right flank of female BABL/c mice (6–8 weeks old). The tumor-bearing mice were randomly divided into groups to investigate biodistribution and tumor targeting efficacy ($n = 4$). Upon reaching a tumor volume of 200 mm^3, the mice received intravenously administration of either free IR780 or IR780-LP at a dose of 100 μg/kg. Under anesthesia, all the mice were monitored in real-time using the IVIS Lumina system (PerkinElmer Inc., Waltham, MA, USA) at 1, 2, 4, 9, 12, 24, 48, and 72 h post-injection. After 72 h, the primary tumor and critical organs (heart, lung, liver, spleen, and kidney) were collected for *ex vivo* imaging.

2.12. Investigation of anti-tumor efficiency

To assess the anti-tumor efficacy and safety of our liposomal formulations, we randomly assigned 8 mice to different groups and administered with free oxaliplatin or liposomes intravenously at day 8, 11,14, and 17. In addition, ADU-S100 was intratumorally injected at day 12 post tumor inoculation. The dose of OXA and ADU-S100 was fixed at 5 mg/kg and 50 μg/mice, respectively. During the treatment, tumor volume and body weight were precisely recorded using a caliper and weighing scale. The formula $V = L \times W \times H$ (L = the length; W = the width; and H = the height of the tumor) was used to calculate the tumor volume. The survival time of the mice was analyzed using Kaplan–Meier survival curves.

2.13. Blood analysis

To monitor the immune response in the circulation, the level of immune cells ($CD3^+$, $CD4^+$, $CD8^+$ T cells, B cells) in the blood was evaluated at day 11 and day 16 post tumor inoculation. After collecting 30 μL of blood *via* a caudal vein puncture, erythrocytes were removed using lysis buffer (clone 17A2, eBioscience). Next, the cells were stained with CD45.2-APC-eFluor780 (clone 104, Thermo Fisher), CD3-BV421 (clone 17A2, Biolegend), CD4-BV711 (clone RM4–5, Biolegend), CD8a-APC-R700 (clone 53–6.7, BD Bioscience), CD19-BV650 (clone 6D5, Thermo Fisher), and CD86-APC (clone GL1, Thermo Fisher). After three washes, the cells were analyzed by flow cytometry (Aurora, Cytek®, Amsterdam, the Netherlands), and the data was processed by FlowJo 10.0 software. Analysis was measured in triplicate.

2.14. Histology and immunohistochemistry

We examined the morphology and necrosis of the CT26 colon tumors by performing the histological examination on 5 μm-thick sections of paraffin-embedded tissue samples. The sections were then stained with hematoxylin and eosin (H&E) for morphological assessment. For immunohistochemical (IHC) staining, an anti-Ki67 mouse antibody (Invitrogen) was used following the manufacturer's protocol. Briefly, the paraffin-embedded sections were deparaffinized with xylene and rehydrated in a graded ethanol series at room temperature, followed by blocking endogenous peroxidase activity with 0.3% H_2O_2 in dH_2O for

10 min. After washing with dH_2O, the sections were pretreated with boiling citrate buffer for 10 min. Next, the sections were blocked with 5% bovine serum albumin (BSA) in PBS for 30 min and then incubated with the primary antibodies (anti-Ki67) at 4 °C overnight. Following three washes in 0.1% Tween/PBS, sections were incubated with the secondary antibody Impress goat anti-rat IgG (horseradish peroxidase) at room temperature for 30 min and incubated with a DAB system for 1 min. The immunoreaction was quenched when brown precipitates formed following incubation in diaminobenzidine. The sections were subsequently counterstained with Mayer's hemalum solution (1:4) in dH2O for 1 min. Finally, the sections were visualized by using a Pannoramic 250 (3DHISTECH, Budapest, Hungary).

2.15. Tumor microenvironment analysis

After treatments, the mice were sacrificed on day 16 to collect tumor samples. The tumors were dissected into smaller pieces using sterile scissors and forceps and then subjected to incubation with Liberase TL (Roche, Mannheim, Germany) in a serum-free RPMI 1640 medium at 37 °C for 30 min. Single-cell suspensions were obtained from the tissues by gently homogenizing the fragments through a 70 μm cell strainer (Falcon, NY, USA). Subsequently, equal portions of the cells were stained with two different antibody panels for analysis. The lymphoid marker panel consisted of anti-CD45.2-PerCP-Cy5.5 (clone 104, Thermo Fisher), anti-CD3e-BV421 (clone 17A2, Biolegend), anti-CD4-BV711 (clone RM4–5, Biolegend), anti-CD8α-APC-R700 (clone 53–6.7, BD Bioscience), anti-CD19-BV650 (clone 6D5, Thermo Fisher), anti-GranB-APC (clone QA16A02, Biolegend), anti-IFN-γ-PE-Cy7 (clone B27, Biolegend), anti-IL-2-BV605 (clone JES6-5H4, Biolegend), and anti-TNF-α-FITC (clone MP6-XT22, Biolegend). The myeloid marker panel consisted of anti-CD45.2-PerCP-Cy5.5, anti-CD11b-eFluo450 (clone M1/70, BD Biosciences), anti-F4/80-PE-Cy5 (clone BM8, Biolegend), anti-Ly6G-BV785 (clone 1A8, Biolegend), anti-Ly6C-BV605 (clone HK1.4, Biolegend), anti-CD11c-APC-eFluo780 (clone HL3, Thermo Fisher), anti-CD40-PE (clone 3/23, BD Biosciences), anti-CD86-APC (clone GL1, Thermo Fisher), and anti-CD206-BV421 (clone C068C2, Biolegend). Flow cytometry (Aurora, Cytek®, Amsterdam, the Netherlands) was used to measure the expression of cell markers, and the data was analyzed using FlowJo 10.0 software.

2.16. Statistical analysis

Data were presented as mean ± standard deviation of the results obtained from our experiments. One- and two-way analysis of variance were used to make multiple comparisons. Bonferroni posttests were performed when comparing all groups *In vivo* tumor treatment studies were repeated in two independent experiments to ensure adequate sample size and reproducibility. All statistical analyses were performed using GraphPad Prism software. The level of statistical significance was noted as follows: *, $p < 0.05$, **, $p < 0.01$, ***, $p < 0.001$, ****, $p < 0.0001$.

3. Results and discussion

3.1. Preparation and characterization of liposomes

In an effort to reduce the associated side effects and improve the drug accumulation in the target site, liposomes were used to deliver oxaliplatin *via* a thin-film hydration method. The resulting liposomes (OLP) contain oxaliplatin in the concentric hydrophilic core with a DL% of approximately 2.6% and a diameter of 122 nm (Table S1& S2), which is ideal for tumor penetration. The coating of PEG and the slightly negative charge enable OLP to circulate in the blood circulation continuously with decreased nonspecific binding, antibody opsonization, and hemolysis [30]. The TEM photographs in Fig. 2A showed that the liposomes were uniformly dispersed and spherical, with a clear structure comprising lipid-bilayer (white area) and aqueous core (grey area). In these liposomes, the presence of DSPC contributed to their stability by packing the lipid tails more densely when the environment temperature was lower than the translational temperature [31]. In addition, we investigated the release behavior of OXA and OLP in the physiological environment (pH 7.4) at 37 °C. As shown in Fig. 2C and Fig. S1, oxaliplatin exhibited a burst release to 90% within 2 h, whereas OLP displayed sustained oxaliplatin release from the liposomes over a period of 72 h and exhibited more release in the acidic environment. These results imply that OLP could protect the payload from environmental degradation and clearance in a long-term circulation and gradually release the drug in a controlled way, which could reduce the administration frequency and lead to improved therapeutic effects.

3.2. Internalization and biodistribution of liposomes

Liposomes are commonly used to efficiently deliver cargo to specific cell types. By means of endocytosis, liposomes can enter the cells due to their high affinity of liposomes with the cell membrane *via* different receptors such as clathrin, and caveolae, *etc.* To assess delivery efficiency, we labeled liposomes with the lipophilic fluorescent dye IR780 to quantify delivery efficiency. As indicated in Fig. 3A, IR780-LP penetrated tumor cells faster and increased over time, with a dose-dependent response. Notably, independent of concentration and time point, IR780-

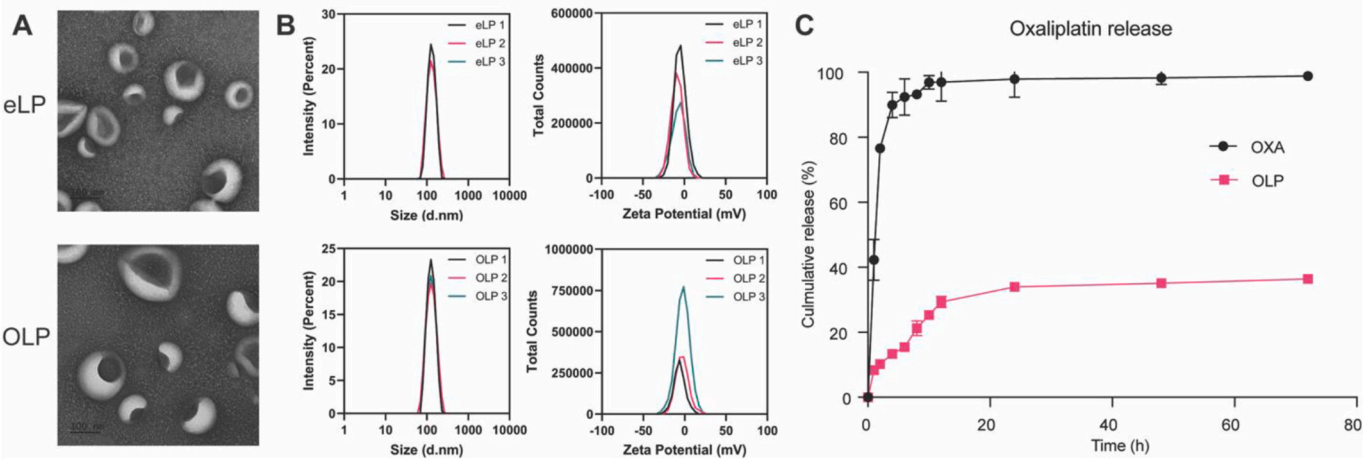

Fig. 2. The characterization of liposomes. A. TEM (transmission electron microscopy) images of eLP (empty liposomes) and OLP (oxaliplatin-loaded liposomes). B. Size and zeta potential distribution of liposomes. C. *In vitro* cumulative release behaviors of free oxaliplatin and OLP.

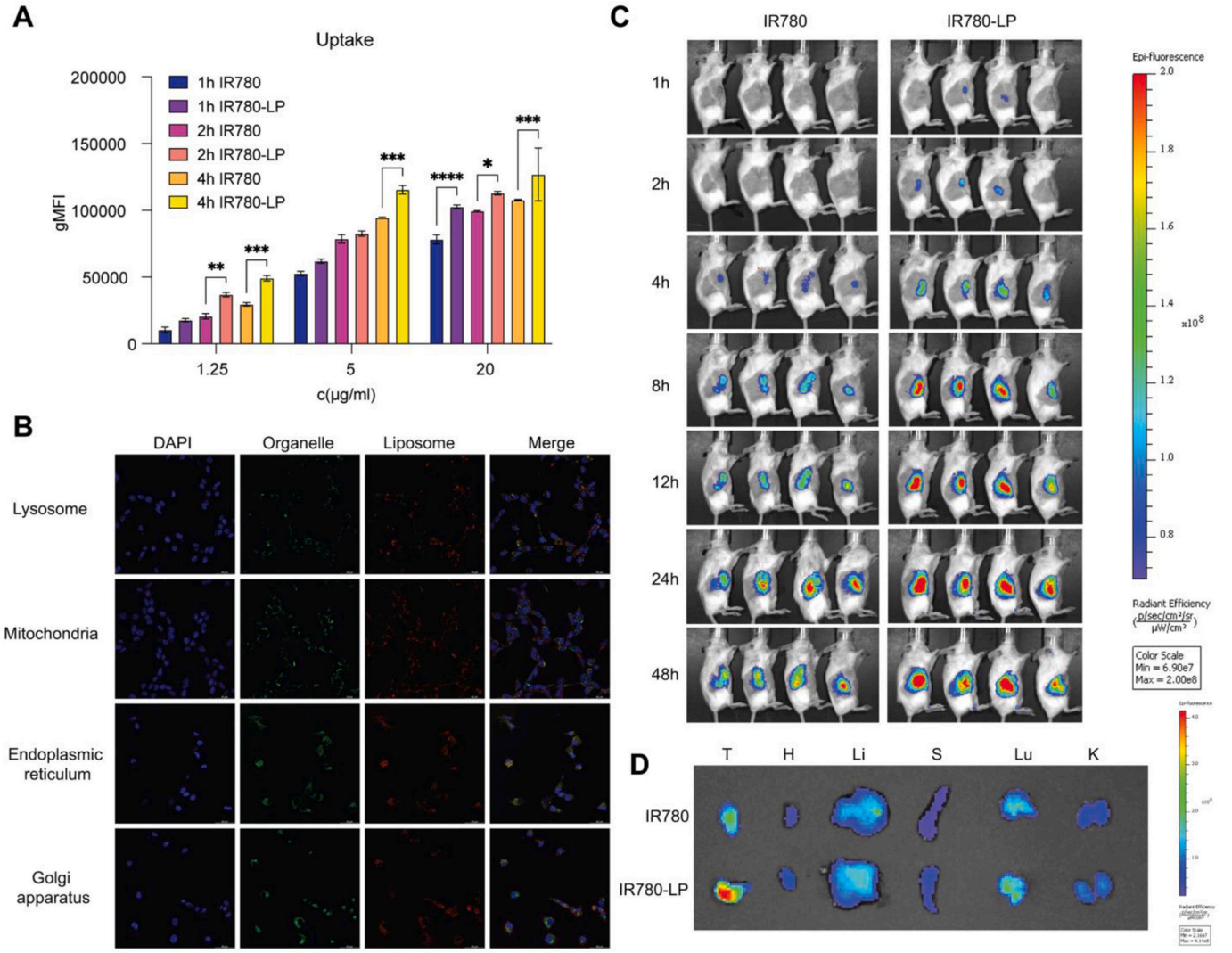

Fig. 3. Cellular internalization of biodistribution of liposomes. A. Quantification of intracellular uptake of free IR780 and IR780-LP ($n = 3$, results were shown in mean ± S.D., *, $p < 0.05$, **, $p < 0.01$, ***, $p < 0.001$, ****, $p < 0.0001$). B. Co-localization of liposomes with different types of cellular organelles (lysosome, mitochondria, ER, and Golgi apparatus). C. IVIS images of IR780 and IR780-LP distribution in CT26 tumor-bearing BALB/c mice. D. *Ex vivo* images of free IR780 and IR780-LPs in hearts (H), livers (Li), spleens (S), lungs (Lu), kidneys (K), and tumors (T) at 48 h post-injection.

LP always exhibited a higher internalization than free IR780, encouraging us to investigate the intracellular locations of liposomes. To elucidate the actual place of liposomes inside the tumor cells, we chose four normally involved cellular organelles, including lysosome, mitochondria, endoplasmic reticulum (ER), and Golgi apparatus, and labeled them with fluorescence. We found that after liposomes entered the tumor cell, they tended to accumulate mainly in the lysosome and ER, in accordance with what was previously reported [32,33]. This suggests that liposomes initially colocalize with the lysosome, escape from the endosomal pathway, or are alternatively transported to ER *via* caveolae-mediated endocytosis [34]. Once inside the organelles, liposomes then release the cargo and achieve other biological activities.

With the potential to promote tumor accumulation of payloads, we further measured the real-time biodistribution of liposomes *in vivo* to ascertain their targeting ability. We injected IR780 or IR780-LP intravenously into CT26 tumor-bearing mice and monitored them at predesigned time points. As seen in Fig. 3C, the fluorescence of the IR780 group was negligible at the beginning, gradually increased over time, peaked after 24 h, and decreased afterward. However, the signal from the IR780-LP group was detectable at 1 h post-injection, reached a plateau at 8 h, and remained undiminished until 48 h. Notably, IR780-LP exhibited more vigorous fluorescence intensity than free IR780 at every time point (Fig. S2), which suggests that liposomes could improve the penetration and accumulation of carried cargo within the tumor site and achieve stable long-term retention. In addition, this superior targeting ability of liposomes was also confirmed by *ex vivo* images of tumors and major organs (Fig. 3D), where IR780-LPs demonstrated a higher intertumoral accumulation than free IR780. Taken together, these results show that liposomes selectively targeted the tumor site by the extended penetration and retention effects, which provide solid evidence for their efficient use in cancer therapy.

3.3. Liposomes enhanced cytotoxicity in vitro

As shown in Fig. 4A, cells treated with eLP exhibited no detectable cytotoxicity underlining the biocompatibility of our liposomes. The designed lipid concentration of 0.16–100 μg/mL did not impair cell growth. Even at a concentration of 500 μg/mL, the cell survival rate was at 80%, demonstrating the liposomes alone did not suppress cell growth. Conversely, OXA inhibited exhibited dose-dependent inhibition of CT26 cell proliferation, with an IC_{50} of 6.5 and 1.3 μg/mL after 24 h and 48 h incubation, respectively (Fig. 4B). Under the same conditions, OLP

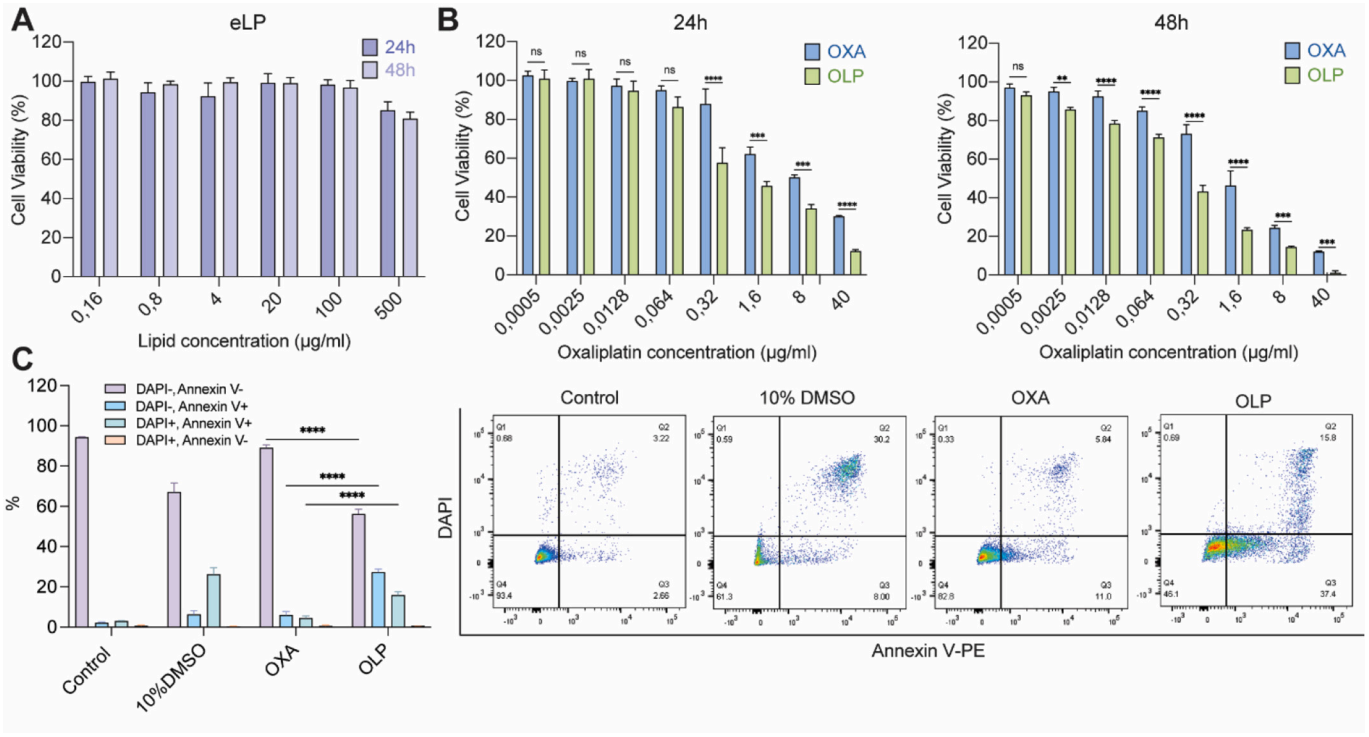

Fig. 4. *In vitro* safety and cytotoxicity of formulations. A. Anti-proliferation assay of CT26 cells treated with eLP after 24 & 48 h ($n = 3$). B. Anti-proliferation assay of CT26 cells treated with OXA and OLP after 24 h and 48 h (n = 3). C. Apoptosis analysis of CT26 cells induced by PBS, 10% DMSO, OXA, and OLP (n = 3, results were shown in mean ± S.D., *, $p < 0.05$, **, $p < 0.01$, ***, $p < 0.001$, ****, $p < 0.0001$).

exhibited significantly higher inhibition of proliferation compared to OXA, especially at the relatively low doses. The IC_{50} of OLP was 5.9-fold and 6.5-fold lower to OXA, which is 1.1 and 0.2 μg/mL after 24 and 48 h, respectively. This improved anti-proliferation effect can be attributed to the increased uptake of the drugs by tumor cells and thus effectively enhanced the inhibitory effect. Furthermore, to assess the induction of apoptosis after treatment, we stained CT26 cells with Annexin-V-PE/DAPI and examined them by flow cytometry (Fig. 4C). The total percentage of apoptosis in the negative control (PBS), positive control (10% DMSO), and free OXA were 5.2 ± 0.3%, 32.5 ± 4.3%, and 10.5 ± 1.9%, respectively. However, cell apoptosis was increased in the OLP groups to 43.2 ± 2.3%, especially in the induction of early apoptosis (Annexin V^+

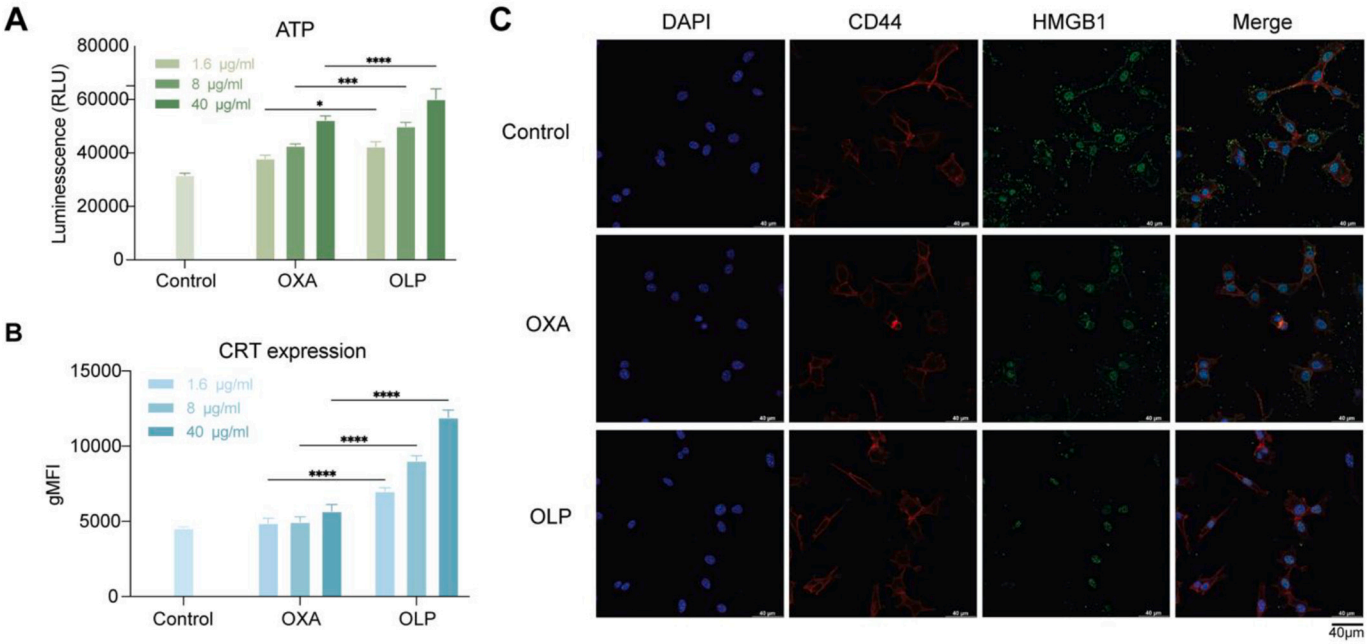

Fig. 5. Liposomes initiate immunogenic cell death. A. ATP released from CT26 cells after 24-h incubation with chemotherapy ($n = 3$). B. CRT expression of CT26 cells after 24-h incubation with chemotherapy (n = 3, results were shown in mean ± S.D., *, $p < 0.05$, **, $p < 0.01$, ***, $p < 0.001$, ****, $p < 0.0001$). C. The translocation of HMGB1 protein of CT26 cells after a 24-h incubation with chemotherapy (scale bar = 40 μm).

DAPI⁻), indicating a significantly stronger apoptotic effect than in other groups. Therefore, these results collectively revealed that liposomes contribute to the promoted cell inhibition and apoptosis.

3.4. Immunogenic cell death induced by liposomes

An immune response can be initiated and activated to eliminate cancer cells through the release of damage-associated molecular patterns (DAMPs) from dying cancer cells. This process is called immunogenic cell death (ICD). It has been reported that chemotherapy-induced ICD can enhance the efficacy of cancer immunotherapy by promoting the recruitment and activation of immune cells within the tumor microenvironment. With low-dose chemotherapy, the systemic immune system appears less affected but exhibits equivalent or even greater antitumor effects [35–37]. We evaluated the ability of liposomes to induce ICD by examining the expression or release of typical DAMPs, including CRT, ATP, and HMGB1. Our results showed OLP induced significantly higher expression of CRT than OXA (Fig. 5A). Similarly, after incubation with OLP, tumor cells released a higher level of ATP into the medium in a dose-dependent manner, whereas OXA nearly induced no ATP release (Fig. 5B & Fig. S3). Confocal microscopy analysis revealed the translocation of HMGB1 from intracellular to extracellular matrix was observed after liposomal treatment (Fig. 5C). We observed that a large amount of HMGB1 was located within tumor cells in control groups. After treatment with free OXA, tumor cells exhibited moderate release of HMGB1. However, nearly no HMGB1 was detected in the cytoplasm of tumor cells in the OLP group, suggesting almost full release of HMGB1 after liposomal treatment. These signals can activate DCs and could synergize with ADU-S100 to amplify the immune response, providing a practical approach to cancer therapy by harnessing the potential of the immune system.

3.5. DC maturation and phagocytosis enhanced by liposome-mediated combination

To determine the optimal dose for activating STING agonist, we first examined the maturation of DCs under different concentrations of ADU-S100 and observed a dose-dependent increase in the expression of costimulatory molecules CD40, CD86, and MHC II, indicating a successful DC maturation (Fig. S4). We also observed an increase in the release of IL-12, a crucial cytokine secreted by DC involved in T cell priming [38,39]. Based on these data, we selected 25 μg/mL of ADU-S100 as an optimal concentration for subsequent *in vitro* experiments due to the practical and economic considerations.

We have demonstrated that treated tumor cells can release and express cues such as ATP and CRT to generate the 'eat me' signal and

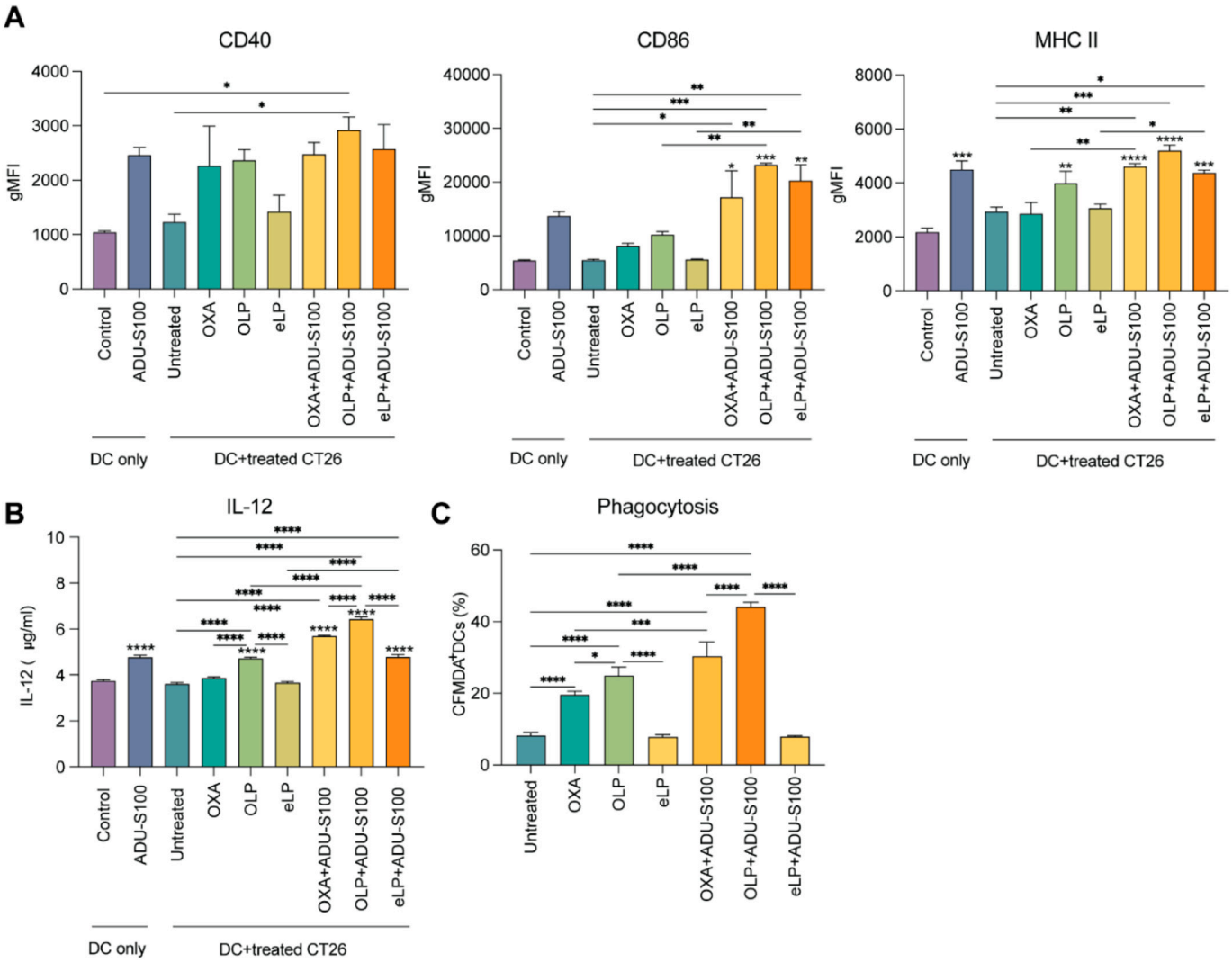

Fig. 6. DC maturation and phagocytosis. A. CD40, CD86, and MHC II expression on DCs after co-culture with treated CT26 cells for 24 h ($n = 3$). B. The release of IL-12 from DCs after co-cultured with treated CT26 cells (n = 3). C. The phagocytosis of DCs after co-cultured with treated CT26 cells (n = 3, results were shown in mean ± S.D., *, $p < 0.05$, **, $p < 0.01$, ***, $p < 0.001$, ****, $p < 0.0001$).

converted the tumor into an *in situ* vaccine [40]. To elucidate how cancer cells interact with DCs, we co-cultured DCs with chemo-treated tumor cells and explored the resulting interactions. This interplay is crucial for the induction of ICD and involves DC maturation as well as phagocytosis of dead cancer cells by DC. When DC maturation is triggered by DAMPs, the upregulation of costimulatory molecules (such as CD40 and CD86) and the release of pro-inflammatory cytokines (such as IL-12) can be detected. Based on this knowledge, we investigated DC maturation markers by flow cytometry and ELISA. Although DCs were not activated upon co-culture with untreated and eLP-treated cancer cells, a moderate increase of CD40, CD80, MHC II was detected after chemotherapy, especially in the OLP group (Fig. 6A & Fig. S5). Cancer cells treated with the liposome-mediated combination (OLP + ADU-S100) induced the highest upregulation of DC maturation markers (*i.e.*, CD40, CD86, and MHC II) among all the groups. Pronounced IL-12 release of DC was observed after co-culture with the liposome-mediated combination, while negligible elevation was found in chemotherapeutic groups. This indicates that the combination of OLP and ADU-S100 could enhance the activation of DCs more efficiently than monotherapy. Furthermore, DCs showed the highest efficiency in engulfing OLP-treated cancer cells under the stimulation of ADU-S100 (Fig. 6C). These results indicate that OLP effectively promotes the

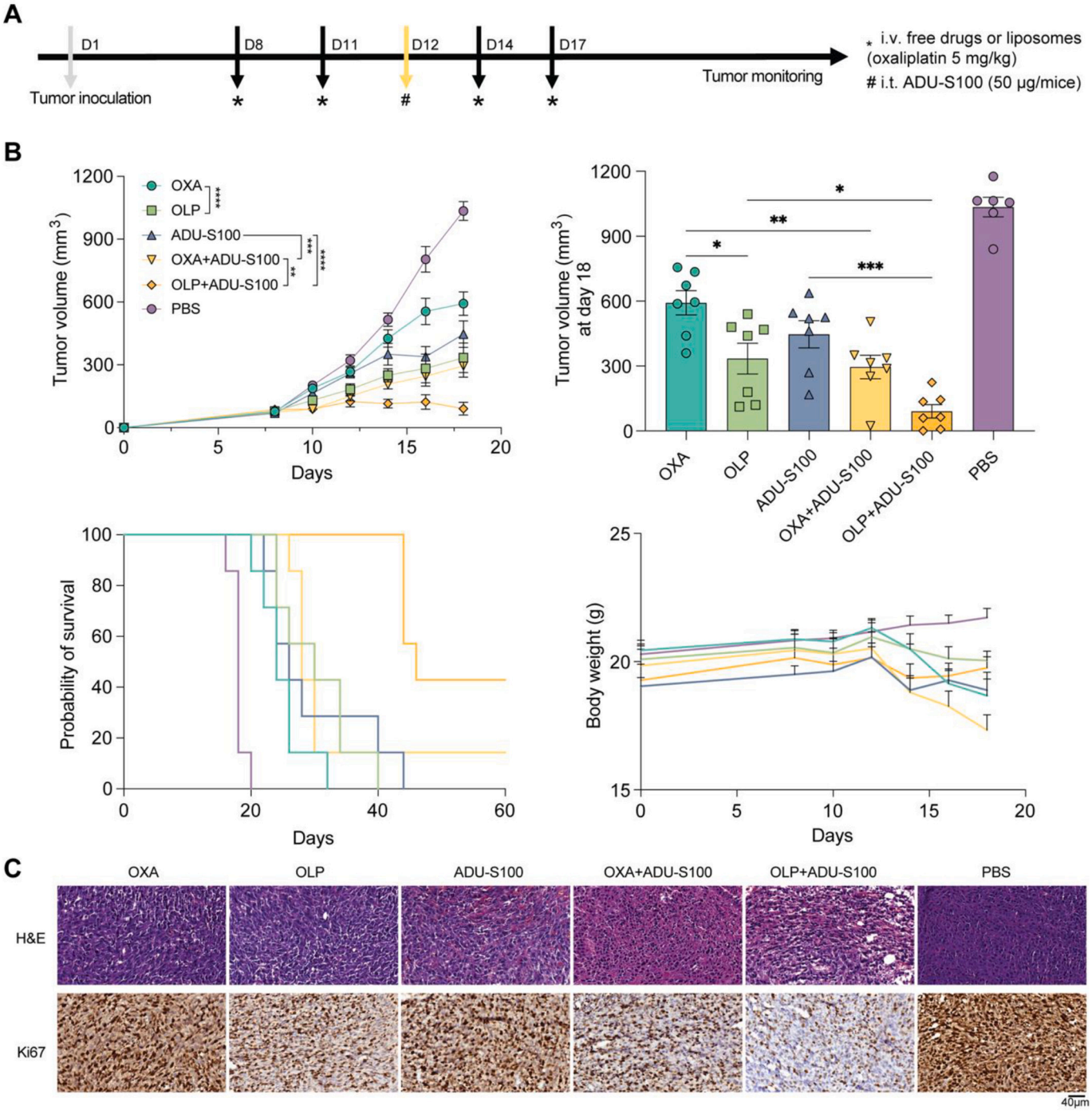

Fig. 7. Anti-tumor effect in the CT26 colorectal cancer model treated with different formulations *in vivo*. A. Schematic illustration of therapeutic schedules against CT26 tumors. B. The tumor growth curve, average tumor volume, body weight, survival rates of mice after multiple treatments ($n = 8$, results were shown in mean ± S.D., *, $p < 0.05$, **, $p < 0.01$, ***, $p < 0.001$, ****, $p < 0.0001$). C. Histological investigation (H&E and Ki67 staining) of different groups. (Scale bar = 40 μm).

release of DAMPs from cancer cells, subsequently triggering the maturation of DCs and enhancing their phagocytosis together with ADU-S100, which can further lead to potent T cell activation.

3.6. Anti-tumor effect in vivo

To assess the effect of liposome-mediated combinational strategy on tumor growth, we treated CT26 tumor-bearing mice with PBS, free OXA, OLP, free OXA + ADU-S100, or OLP + ADU-S100 and monitored them over time. The dose and injection frequency are illustrated in Fig. 7A. After giving chemotherapy every two days for a total of 4 treatments, the tumor growth could be partially inhibited, but the tumor inhibition was still insufficient. With only one local administration of ADU-S100, we observed that the immunochemotherapy substantially inhibited tumor growth and increased survival significantly (Fig. 7B). Notably, the liposome-involved group exhibited much higher tumor inhibition than the corresponding free drug group, whether used as monotherapy or combinational therapy. As expected, only OLP + ADU-S100 achieved a complete regression of the tumor. This improved anti-tumor response is directly translated into a superior survival benefit with an 86% increase in median survival compared to treatment with free ADU-S100 alone. Additionally, histological examinations further confirmed the decreased tumor burden on mice receiving liposome-mediated combinational treatment. This group had the most tissue damage and the lowest cell

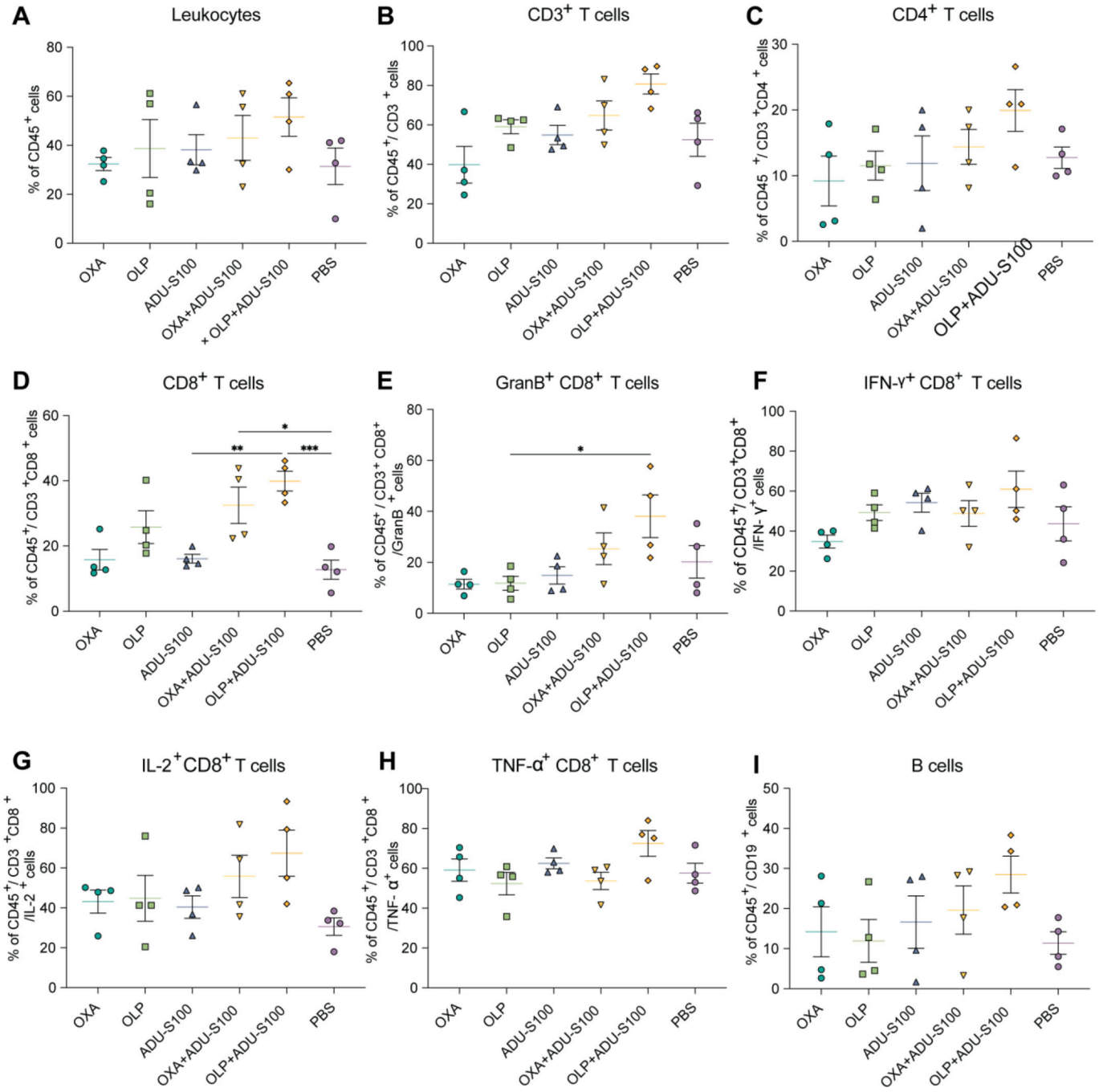

Fig. 8. Lymphocyte populations in the TME after different treatments. Percentage of CD45 + leukocytes (A), $CD3^+$ T cells (B), $CD4^+$T cells (C), $CD8^+$ T cells (D), Granzyme B^+ T cells (E), IFN-γ^+CD8^+T cells (F), IL-2^+ T cells (G), TNF-α^+CD8^+ T cells (H), B cells (I) in the TME. ($n = 4$, results were shown in mean ± S.D., *, $p < 0.05$, **, $p < 0.01$, ***, $p < 0.001$, ****, $p < 0.0001$).

proliferation, as well as clear chromatin condensation, cell/tissue structure shrinkage, and downregulated expression of Ki67 (Fig. 7C). This observation suggests a superior alleviation of the tumor burden induced by the combination of OLP and STING agonist. With the controlled release and passive targeting ability of liposomes, oxaliplatin can be effectively delivered to tumor sites with an improved penetration, consequently improving its bioavailability. Once oxaliplatin enters tumor cells and induces the release of DAMPs as well as dsDNA, DC activation, which initiates anti-tumor immunity, can be effectively amplified by ADU-S100, subsequently increasing the recruitment and infiltration of T lymphocytes and regulate other types of immune cells. Hence, our liposome-based immunochemotherapy provides compelling evidence for its superior anticancer efficacy in CT26 colorectal cancer.

3.7. Improved systemic and local anti-tumor response

We evaluated the effect of liposome-based combinational therapy on the generation of anti-tumoral adaptive immune responses by measuring the levels of circulating T lymphocytes and B lymphocytes in the blood of mice 11 and 16 days after inoculation with CT26 tumors. As shown in Fig. S6, it was observed that the percentage of $CD3^+$ and $CD8^+$ T cells was initially enhanced by chemotherapy before the administration of STING agonist. At day 11, the average number of $CD3^+$ and $CD8^+$ T cells was higher in the blood of mice treated with OLP than in mice treated with OXA only, but this difference was not statistically significant (Figs. S6 B & D). However, upon the administration of ADU-S100, at day 16, the number of circulating $CD3^+$T cells, $CD8^+$ T cells, and $CD86^+$ B cells was significantly increased (Fig. S6B, D, &F). These data indicated the importance of administration sequence: inducing stimuli *in situ* by chemotherapy and then amplifying the anti-tumor immunity by immune adjuvants.

Furthermore, to assess the potential of liposome-based immunochemotherapy to alter the TME and enhance anti-tumor efficacy *in vivo*, we also evaluated its capability of immune activation by measuring both the level and function of immune cells. We analyzed treated tumor tissues through flow cytometry and noted a moderate increase in the population of $CD45^+$ leukocytes, $CD3^+$ T cells, and $CD4^+$ T cells after being treated with monotherapy (Fig. 8A-C). With the treatment of immunochemotherapy, the percentage of all T lymphocytes and B lymphocytes significantly increased, especially in the liposome-involving groups (Fig. 8A-D). Furthermore, it has been revealed that activated T cells take different pathways to eliminate tumor cells, including secreting TNF-α and IFN-γ and cytotoxic granules [41–43]. Also, IL-2 is a key regulator of T cell metabolic programs to enable the proliferation of T cell populations [44]. Given their crucial role in the cytotoxic process, we expected elevated expression after immunotherapy treatment. We observed a robust population of granzyme B^+ $CD8^+$ T cells in the liposome-based immunotherapy group, suggesting the release of cytotoxic granules activated $CD8^+$ T cells into the extracellular space to kill tumor cells (Fig. 8E). Additionally, robust IL-2, IFN-γ and TNF-α responses were observed in mice treated with OLP + ADU-S100 (Fig. 8F-H). These results together demonstrated the liposome-mediated chemotherapy together with local STING activation, recruited cytotoxic T lymphocytes with a superior efficiency among all the other groups. In addition, we also found this treatment enhanced the percentage of B cells in comparison to the control, which further improved the anti-tumor effects. Together, these results provide strong evidence that liposome-based immunochemotherapy activates adaptive immune responses *via* improved maturation of DCs, STING-mediated T cell priming and provide a rationale for the use of chemotherapy in combination with immune regiments to generate strong and effective anti-tumor responses.

3.8. Intratumoral immune activation

Myeloid cells in the TME are aggressively regulated to suppress anti-tumor T cell responses. With a sizable proportion of myeloid cells, which contain both immunostimulatory and immunosuppressive subsets, tumors can escape the elimination of T cell *via* multiple mechanisms [45–47]. Typically, immunostimulatory myeloid cells such as DCs and M1-subtype macrophages, and myeloid-derived suppressor cells (MDSCs), including M2-subtype macrophages, immature myeloid cells function collectively to modulate the immune response in the TME [48]. Therefore, it is critical for beneficial cancer treatment to deplete MDSCs and/or increase immunostimulatory subsets. To investigate the regulatory effects of liposome-mediated immunotherapy on both adaptive and innate immunity, we analyzed changes in the myeloid population after treatments. As indicated in Fig. 9A, the liposome-mediated immunotherapy induced the highest recruitment of mature DCs ($CD40^+CD86^+CD11c^+$) to the TME, which provided an excellent opportunity for the priming of T cells. Similar to DCs, this combination possessed the highest efficiency to induce an acute inflammatory response, which was reflected by the higher level of inflammatory monocytes ($CD11b^+F4/80^+/Ly6G^-Ly6C^{hi}$), though these differences were not significant (Fig. 9B). Moreover, significant differences in both M1- and M2-like macrophage infiltration were observed in the combinational groups when compared to the control or monotherapy. Mice treated with OXA, OLP, ADU-S100, and OXA + ADU-S100 showed 1.6-, 2.5-, 1.7-, and 3.0-fold increase of M1-subtype macrophages ($CD11b^+F4/80^+/CD86^+CD206^-$) compared to the control group, respectively, whereas OLP + AUD-S100 effectively induced a 5.2-fold increase to the control group and a 12-fold elevation of M1/M2 ratio (Fig. 9D & F). The OLP + ADU-S100 group displayed the greatest decrease of M2-subtype macrophages ($CD11b^+F4/80^+/CD86^-CD206^+$) among all the groups, which was 0.45-fold to control (Fig. 9E). Together with the abatement of M2-subtype macrophages, the diminishment of immature myeloid ($CD11b^+Ly6G^-Ly6C^{hi}$)) in the liposome-based immunochemotherapy further assisted with the normalization of immunosuppressive TME (Fig. 9C). Overall, these results show that the addition of liposome-based chemotherapy to STING activation leads to a significant augment in immunostimulatory subsets and a decrease in MDSCs recruitment into the microenvironment.

Regulatory T lymphocytes (Tregs), another type of immune cells, suppress anti-tumor immunity by modulating the activation and differentiation of conventional CD4+ T cells and other cell lineages within the innate and adaptive immune system [49]. It has been reported that Treg depletion was linked to the strong anti-tumor effects by increasing the number of $CD4^+$ and/or $CD8^+$ effector T cells within the tumor, leading to potent anti-tumor effects [50]. The elimination of Treg-mediated inhibition in the TME was one of the key strategies for tumor eradication. Therefore, we analyzed the infiltration of Tregs in the tumor and spleen after different treatments. After monotherapy with free OXA, OLP, or ADU-S100, the percentage of Tregs in the tumor was 65.5%, 57.2%, and 56,9%, respectively, slightly decreasing from the 66.3% of the control group (Fig. 9 G&H). However, a robust reduction of Tregs (23.4%) was observed in the liposome-mediated immunochemotherapy, lower than the 36.1% of corresponding free combination. A similar trend was observed in splenocytes (Fig. S7), indicating additional aid of liposomes in enhancing anti-tumor immunity *via* eliminating Tregs. Hence, the strengthened anti-tumor responses induced by liposome-mediated immunochemotherapy also correlated with the depletion of Tregs.

4. Conclusion

The development of a novel liposome-mediated immunochemotherapy strategy offers a promising solution to overcome the current limitations of STING agonists and chemotherapy. By delivering high concentrations of oxaliplatin to induce ICD in the tumor site and activate DCs alongside ADU-S100, this approach enables targeted and localized immune activation with minimal systemic effects. The synergistic effect of this combinational strategy leads to improved CTLs infiltration and

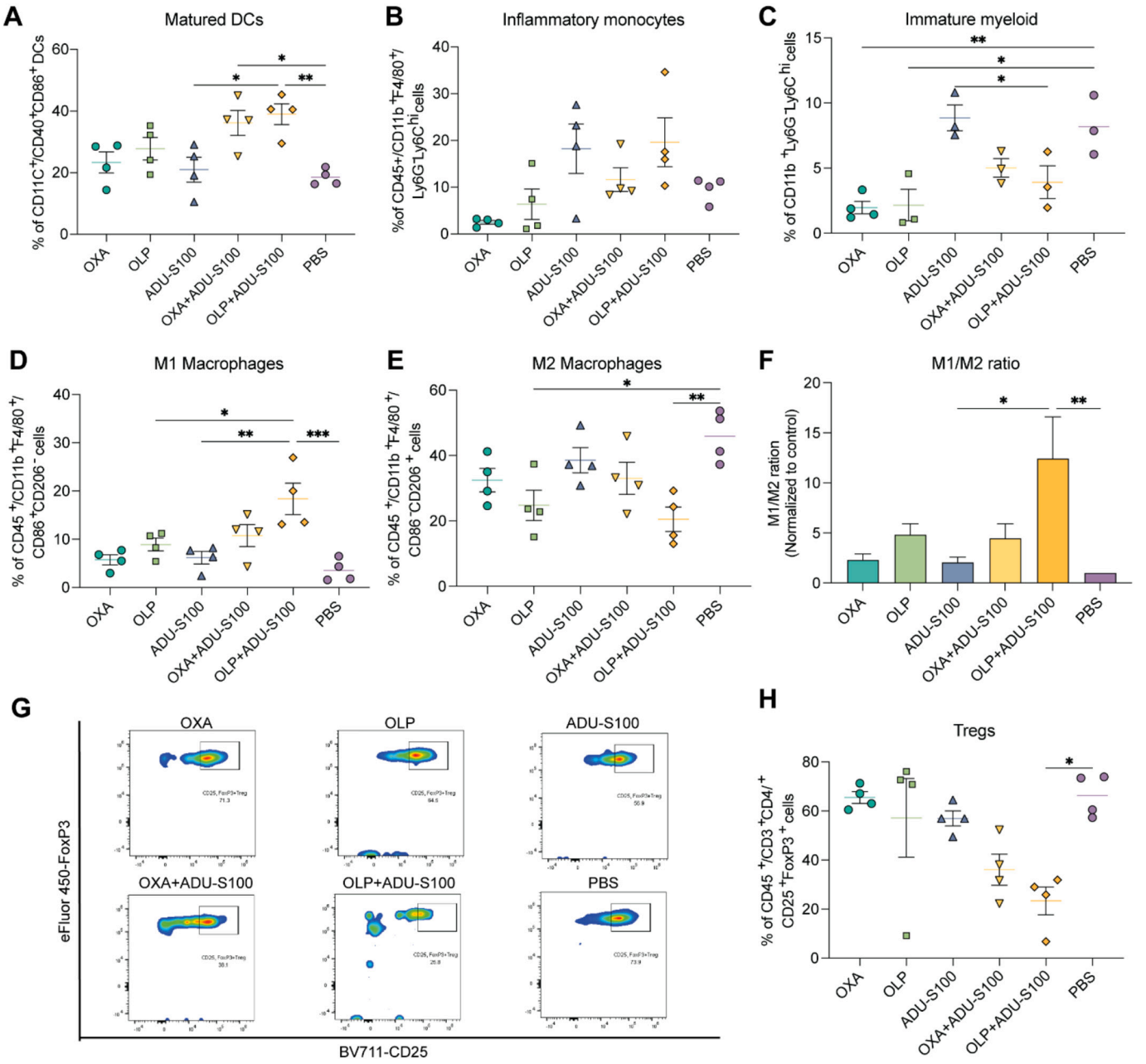

Fig. 9. Myeloid populations and Tregs in the TME after treatments. Percentage of matured DCs (A), inflammatory monocytes (B), immature myeloid (C), M1 macrophages (D), M2 macrophages (E), M1/M2 ratio (F), and Tregs (H) and the population of Tregs (G) in the tumor microenvironment. ($n = 4$, results were shown in mean ± S.D., *, $p < 0.05$, **, $p < 0.01$, ***, $p < 0.001$, ****, $p < 0.0001$).

cytotoxicity in primary tumors, converting the tumor into a vaccine *in situ* and releasing DAMPs that amplify anti-tumor immunity *via* STING activation. This liposome-mediated immunochemotherapy provides a platform for the modulation of the TME by bridging innate and adaptive immune responses and eliminating suppressive immune cells, thereby enhancing the effectiveness of cancer immunotherapy. These findings offer a new perspective on the development of future combinations of immune regimens and chemotherapeutic agents that utilize drug delivery systems to improve cancer treatment efficacy while minimizing toxicity.

CRediT authorship contribution statement

Zili Gu: Conceptualization, Data curation, Writing – original draft, Visualization, Investigation. **Yang Hao:** Writing – review & editing. **Timo Schomann:** Visualization, Writing – review & editing. **Ferry Ossendorp:** Writing – review & editing. **Peter ten Dijke:** Writing – review & editing, Supervision. **Luis J. Cruz:** Writing – review & editing, Supervision.

Declaration of Competing Interest

The authors declare no conflicts of interest.

Data availability

No data was used for the research described in the article.

Acknowledgements

The authors thank the financial support from the European Union's Horizon 2020 research and innovation program under the Marie Sklodowska Curie grant agreement No 777682 (CANCER), 734684 (CHARMED), 872860 (PRISAR2); 807281(ACORN), 852985 (SIMICA), 952520 (BIOSAFETY), 861190 (PAVE), 857894 (CAST), 859908 (NOVA-MRI), 956477 (PIANO). Yang Hao was funded by Jilin Province Chinese Postdoctoral International Exchange Program (Grant No. YJ20220406).

Appendix A. Supplementary data

Supplementary data to this article can be found online at https://doi.org/10.1016/j.jconrel.2023.04.011.

References

[1] Y. Zhang, Z. Zhang, The history and advances in cancer immunotherapy: understanding the characteristics of tumor-infiltrating immune cells and their therapeutic implications, Cell. Mol. Immunol. 17 (2020) 807–821, https://doi.org/10.1038/s41423-020-0488-6.
[2] R.M. Steinman, I. Mellman, Immunotherapy: bewitched, bothered, and bewildered no more, Science 305 (2004) (1979) 197–200, https://doi.org/10.1126/science.1099688.
[3] D.N. Khalil, E.L. Smith, R.J. Brentjens, J.D. Wolchok, The future of cancer treatment: immunomodulation, CARs and combination immunotherapy, Nat. Rev. Clin. Oncol. 13 (2016) 273–290, https://doi.org/10.1038/nrclinonc.2016.25.
[4] J.J. Luke, K.T. Flaherty, A. Ribas, G.V. Long, Targeted agents and immunotherapies: optimizing outcomes in melanoma, Nat. Rev. Clin. Oncol. 14 (2017) 463–482, https://doi.org/10.1038/nrclinonc.2017.43.
[5] K. Ganesh, Z.K. Stadler, A. Cercek, R.B. Mendelsohn, J. Shia, N.H. Segal, L.A. Diaz, Immunotherapy in colorectal cancer: rationale, challenges and potential, Nat. Rev. Gastroenterol. Hepatol. 16 (2019) 361–375, https://doi.org/10.1038/s41575-019-0126-x.
[6] M. Reck, J. Remon, M.D. Hellmann, First-line immunotherapy for non–small-cell lung Cancer, J. Clin. Oncol. 40 (2022) 586–597, https://doi.org/10.1200/JCO.21.
[7] X. Li, S. Khorsandi, Y. Wang, J. Santelli, K. Huntoon, N. Nguyen, M. Yang, D.Y. Lee, Y. Lu, R. Gao, B.Y.S. Kim, C. de Gracia Lux, R.F. Mattrey, W. Jiang, J. Lux, Cancer immunotherapy based on image-guided STING activation by nucleotide nanocomplex-decorated ultrasound microbubbles, Nat. Nanotechnol. 17 (2022) 891–899, https://doi.org/10.1038/s41565-022-01134-z.
[8] D.Y. Lee, K. Huntoon, Y. Wang, W. Jiang, B.Y.S. Kim, Harnessing innate immunity using biomaterials for Cancer immunotherapy, Adv. Mater. 33 (2021), https://doi.org/10.1002/adma.202007576.
[9] J. Zheng, J. Mo, T. Zhu, W. Zhuo, Y. Yi, S. Hu, J. Yin, W. Zhang, H. Zhou, Z. Liu, Comprehensive elaboration of the cGAS-STING signaling axis in cancer development and immunotherapy, Mol. Cancer 19 (2020), https://doi.org/10.1186/s12943-020-01250-1.
[10] J.K. Won, S.F. Bakhoum, The cytosolic DNA-sensing cGAS–sting pathway in cancer, Cancer Discov. 10 (2020) 26–39, https://doi.org/10.1158/2159-8290.CD-19-0761.
[11] M. Jiang, M. Jiang, P. Chen, P. Chen, L. Wang, W. Li, B. Chen, Y. Liu, Y. Liu, H. Wang, H. Wang, S. Zhao, L. Ye, Y. He, C. Zhou, cGAS-STING, an important pathway in cancer immunotherapy, J. Hematol. Oncol. 13 (2020), https://doi.org/10.1186/s13045-020-00916-z.
[12] R. Zhang, R. Kang, D. Tang, The STING1 network regulates autophagy and cell death, Signal Transduct Target Ther. 6 (2021), https://doi.org/10.1038/s41392-021-00613-4.
[13] Y.S. Tan, K. Sansanaphongpricha, Y. Xie, C.R. Donnelly, X. Luo, B.R. Heath, X. Zhao, E. Bellile, H. Hu, H. Chen, P.J. Polverini, Q. Chen, S. Young, T.E. Carey, J. E. Nor, R.L. Ferris, G.T. Wolf, D. Sun, Y.L. Lei, Mitigating SOX2-potentiated immune escape of head and neck squamous cell carcinoma with a STING-inducing nanosatellite vaccine, Clin. Cancer Res. 24 (2018) 4242–4255, https://doi.org/10.1158/1078-0432.CCR-17-2807.
[14] L. Ding, Q. Wang, A. Martincuks, M.J. Kearns, T. Jiang, Z. Lin, X. Cheng, C. Qian, S. Xie, H.-J. Kim, I.-M. Launonen, A. Färkkilä, T.M. Roberts, G.J. Freeman, J.F. Liu, P.A. Konstantinopoulos, U. Matulonis, H. Yu, J.J. Zhao, STING agonism overcomes STAT3-mediated immunosuppression and adaptive resistance to PARP inhibition in ovarian cancer, J Immunother Cancer. 11 (2023), e005627, https://doi.org/10.1136/jitc-2022-005627.
[15] L. Wang-Bishop, M. Wehbe, D. Shae, J. James, B.C. Hacker, K. Garland, P. P. Chistov, M. Rafat, J.M. Balko, J.T. Wilson, Potent STING activation stimulates immunogenic cell death to enhance antitumor immunity in neuroblastoma, J Immunother Cancer. 8 (2020), https://doi.org/10.1136/jitc-2019-000282.
[16] S. Chattopadhyay, Y.H. Liu, Z.S. Fang, C.L. Lin, J.C. Lin, B.Y. Yao, C.M.J. Hu, Synthetic immunogenic cell death mediated by intracellular delivery of STING agonist Nanoshells enhances anticancer chemo-immunotherapy, Nano Lett. 20 (2020) 2246–2256, https://doi.org/10.1021/acs.nanolett.9b04094.
[17] S.J. Paston, V.A. Brentville, P. Symonds, L.G. Durrant, Cancer vaccines, adjuvants, and delivery systems, Front. Immunol. 12 (2021), https://doi.org/10.3389/fimmu.2021.627932.
[18] M. Lopez-Pelaez, L. Young, M. Vazquez-Chantada, N. Nelson, S. Durant, R. W. Wilkinson, E. Poon, M. Gaspar, V. Valge-Archer, P. Smith, S.J. Dovedi, Targeting DNA damage response components induces enhanced STING-dependent type-I IFN response in ATM deficient cancer cells and drives dendritic cell activation, Oncoimmunology. 11 (2022), https://doi.org/10.1080/2162402X.2022.2117321.
[19] E.M. Barros, S.A. McIntosh, K.I. Savage, The DNA damage induced immune response: implications for cancer therapy, DNA Repair (Amst) 120 (2022), https://doi.org/10.1016/j.dnarep.2022.103409.
[20] N. Casares, M.O. Pequignot, A. Tesniere, F. Ghiringhelli, S. Roux, N. Chaput, E. Schmitt, A. Hamai, S. Hervas-Stubbs, M. Obeid, F. Coutant, D. Métivier, E. Pichard, P. Aucouturier, G. Pierron, C. Garrido, L. Zitvogel, G. Kroemer, Caspase-dependent immunogenicity of doxorubicin-induced tumor cell death, J. Exp. Med. 202 (2005) 1691–1701, https://doi.org/10.1084/jem.20050915.
[21] H. Arai, Y. Xiao, F. Loupakis, N. Kawanishi, J. Wang, F. Battaglin, S. Soni, W. Zhang, C. Mancao, B. Salhia, S.M. Mumenthaler, D.J. Weisenberger, G. Liang, C. Cremolini, A. Falcone, J. Millstein, H.J. Lenz, Immunogenic cell death pathway polymorphisms for predicting oxaliplatin efficacy in metastatic colorectal cancer, J Immunother Cancer. 8 (2020), https://doi.org/10.1136/jitc-2020-001714.
[22] C.G. da Silva, F. Rueda, C.W. Löwik, F. Ossendorp, L.J. Cruz, Combinatorial prospects of nano-targeted chemoimmunotherapy, Biomaterials. 83 (2016) 308–320, https://doi.org/10.1016/j.biomaterials.2016.01.006.
[23] J.M. Woynarowski, S. Faivre, M.C.S. Herzig, B. Arnett, W.G. Chapman, A. V. Trevino, E. Raymond, S.G. Chaney, A. Vaisman, M. Varchenko, P.E. Juniewicz, Oxaliplatin-Induced Damage of Cellular DNA. http://www.molpharm.org, 2000.
[24] S. Faivre, D. Chan, R. Salinas, B. Woynarowska, J.M. Woynarowski, DNA strand breaks and apoptosis induced by oxaliplatin in cancer cells, Biochem. Pharmacol. 66 (2003) 225–237, https://doi.org/10.1016/S0006-2952(03)00260-0.
[25] F. Li, X. Zheng, X. Wang, J. Xu, Q. Zhang, Macrophage polarization synergizes with oxaliplatin in lung cancer immunotherapy via enhanced tumor cell phagocytosis, Transl. Oncol. 14 (2021), https://doi.org/10.1016/j.tranon.2021.101202.
[26] R. Ma, T. Ji, D. Chen, W. Dong, H. Zhang, X. Yin, J. Ma, X. Liang, Y. Zhang, G. Shen, X. Qin, B. Huang, Tumor cell-derived microparticles polarize M2 tumor-associated macrophages for tumor progression, Oncoimmunology. 5 (2016), https://doi.org/10.1080/2162402X.2015.1118599.
[27] L. Corrales, L.H. Glickman, S.M. McWhirter, D.B. Kanne, K.E. Sivick, G.E. Katibah, S.R. Woo, E. Lemmens, T. Banda, J.J. Leong, K. Metchette, T.W. Dubensky, T. F. Gajewski, Direct activation of STING in the tumor microenvironment leads to potent and systemic tumor regression and immunity, Cell Rep. 11 (2015) 1018–1030, https://doi.org/10.1016/j.celrep.2015.04.031.
[28] Z. Gu, C.G. da Silva, K. van der Maaden, F. Ossendorp, L.J. Cruz, Liposome-based drug delivery systems in cancer immunotherapy, Pharmaceutics. 12 (2020) 1–25, https://doi.org/10.3390/pharmaceutics12111054.
[29] Z. Gu, C.G. da Silva, Y. Hao, T. Schomann, M.G.M. Camps, K. van der Maaden, Q. Liu, F. Ossendorp, L.J. Cruz, Effective combination of liposome-targeted chemotherapy and PD-L1 blockade of murine colon cancer, J. Control. Release 353 (2023) 490–506, https://doi.org/10.1016/j.jconrel.2022.11.049.
[30] Z. Gu, C.G. da Silva, Y. Hao, T. Schomann, M.G.M. Camps, K. van der Maaden, Q. Liu, F. Ossendorp, L.J. Cruz, Effective combination of liposome-targeted chemotherapy and PD-L1 blockade of murine colon cancer, J. Control. Release 353 (2023) 490–506, https://doi.org/10.1016/j.jconrel.2022.11.049.
[31] D. Drabik, G. Chodaczek, S. Kraszewski, M. Langner, Mechanical properties determination of DMPC, DPPC, DSPC, and HSPC solid-ordered bilayers, Langmuir. 36 (2020) 3826–3835, https://doi.org/10.1021/acs.langmuir.0c00475.
[32] R.N. Majzoub, C.L. Chan, K.K. Ewert, B.F.B. Silva, K.S. Liang, C.R. Safinya, Fluorescence microscopy colocalization of lipid-nucleic acid nanoparticles with wildtype and mutant Rab5-GFP: a platform for investigating early endosomal events, Biochim. Biophys. Acta Biomembr. 2015 (1848) 1308–1318, https://doi.org/10.1016/j.bbamem.2015.03.001.
[33] N. Duzgunes, D. Duzgunes, S. Nir, Mechanisms and Kinetics of Liposome-Cell Interactions. www.elsevier.com/locate/drugdeliv, 1999.
[34] S. Pollock, R. Antrobus, L. Newton, B. Kampa, J. Rossa, S. Latham, N.B. Nichita, R. A. Dwek, N. Zitzmann, Uptake and trafficking of liposomes to the endoplasmic reticulum, FASEB J. 24 (2010) 1866–1878, https://doi.org/10.1096/fj.09-145755.
[35] L.A. Emens, G. Middleton, The interplay of immunotherapy and chemotherapy: harnessing potential synergies, Cancer, Immunol. Res. 3 (2015) 436–443, https://doi.org/10.1158/2326-6066.CIR-15-0064.
[36] L. Galluzzi, A. Buqué, O. Kepp, L. Zitvogel, G. Kroemer, Immunological effects of conventional chemotherapy and targeted anticancer agents, Cancer Cell 28 (2015) 690–714, https://doi.org/10.1016/j.ccell.2015.10.012.
[37] V. Schirrmacher, From chemotherapy to biological therapy: a review of novel concepts to reduce the side effects of systemic cancer treatment (review), Int. J. Oncol. 54 (2019) 407–419, https://doi.org/10.3892/ijo.2018.4661.
[38] C.J. Henry, D.A. Ornelles, L.M. Mitchell, K.L. Brzoza-Lewis, E.M. Hiltbold, IL-12 Produced by Dendritic Cells Augments CD8+ T Cell Activation through the Production of the Chemokines CCL1 and CCL17 1, 2022.
[39] C.A. Thaiss, V. Semmling, L. Franken, H. Wagner, C. Kurts, Chemokines: a new dendritic cell signal fort cell activation, Front. Immunol. 2 (2011), https://doi.org/10.3389/fimmu.2011.00031.
[40] M.Z. Jin, X.P. Wang, Immunogenic cell death-based Cancer vaccines, Front. Immunol. 12 (2021), https://doi.org/10.3389/fimmu.2021.697964.

[41] P. Bhat, G. Leggatt, N. Waterhouse, I.H. Frazer, Interferon-γ derived from cytotoxic lymphocytes directly enhances their motility and cytotoxicity, Cell Death Dis. 8 (2017), https://doi.org/10.1038/CDDIS.2017.67.
[42] S. Halle, O. Halle, R. Förster, Mechanisms and dynamics of T cell-mediated cytotoxicity in vivo, Trends Immunol. 38 (2017) 432–443, https://doi.org/10.1016/j.it.2017.04.002.
[43] G.Z. Tau, S.N. Cowan, J. Weisburg, N.S. Braunstein, P.B. Rothman, Regulation of IFN-γ signaling is essential for the cytotoxic activity of CD8+ T cells, J. Immunol. 167 (2001) 5574–5582, https://doi.org/10.4049/jimmunol.167.10.5574.
[44] S.H. Ross, D.A. Cantrell, Signaling and function of Interleukin-2 in T lymphocytes, Annu. Rev. Immunol. 36 (2018) 411–433, https://doi.org/10.1146/annurev-immunol-042617-053352.
[45] M.M. Gubin, E. Esaulova, J.P. Ward, O.N. Malkova, D. Runci, P. Wong, T. Noguchi, C.D. Arthur, W. Meng, E. Alspach, R.F.V. Medrano, C. Fronick, M. Fehlings, E. W. Newell, R.S. Fulton, K.C.F. Sheehan, S.T. Oh, R.D. Schreiber, M.N. Artyomov, High-dimensional analysis delineates myeloid and lymphoid compartment remodeling during successful immune-checkpoint cancer therapy, Cell. 175 (2018) 1014–1030.e19, https://doi.org/10.1016/j.cell.2018.09.030.
[46] M.L. Broz, M.F. Krummel, The emerging understanding of myeloid cells as partners and targets in tumor rejection, Cancer, Immunol. Res. 3 (2015) 313–319, https://doi.org/10.1158/2326-6066.CIR-15-0041.
[47] A. Mantovani, F. Marchesi, A. Malesci, L. Laghi, P. Allavena, Tumour-associated macrophages as treatment targets in oncology, Nat. Rev. Clin. Oncol. 14 (2017) 399–416, https://doi.org/10.1038/nrclinonc.2016.217.
[48] F. Veglia, M. Perego, D. Gabrilovich, Myeloid-derived suppressor cells coming of age review-article, Nat. Immunol. 19 (2018) 108–119, https://doi.org/10.1038/s41590-017-0022-x.
[49] D.A.A. Vignali, L.W. Collison, C.J. Workman, How regulatory T cells work, Nat. Rev. Immunol. 8 (2008) 523–532, https://doi.org/10.1038/nri2343.
[50] A.M. Magnuson, E. Kiner, A. Ergun, J.S. Park, N. Asinovski, A. Ortiz-Lopez, A. Kilcoyne, E. Paoluzzi-Tomada, R. Weissleder, D. Mathis, C. Benoist, Identification and validation of a tumor-infiltrating Treg transcriptional signature conserved across species and tumor types, Proc. Natl. Acad. Sci. U. S. A. 115 (2018) E10672–E10681, https://doi.org/10.1073/pnas.1810580115.